nature nanotechnology

LETTERS

PUBLISHED ONLINE: 10 NOVEMBER 2013 | DOI: 10.1038/NNANO.2013.227

High-throughput optical imaging and spectroscopy of individual carbon nanotubes in devices

Kaihui Liu[1†], Xiaoping Hong[1†], Qin Zhou[1], Chenhao Jin[1], Jinghua Li[2], Weiwei Zhou[2], Jie Liu[2], Enge Wang[3], Alex Zettl[1,4] and Feng Wang[1,4]*

Single-walled carbon nanotubes are uniquely identified by a pair of chirality indices (*n*,*m*), which dictate the physical structures and electronic properties of each species[1]. Carbon nanotube research is currently facing two outstanding challenges: achieving chirality-controlled growth and understanding chirality-dependent device physics[2–6]. Addressing these challenges requires, respectively, high-throughput determination of the nanotube chirality distribution on growth substrates and *in situ* characterization of the nanotube electronic structure in operating devices. Direct optical imaging and spectroscopy techniques are well suited for both goals[7–9], but their implementation at the single nanotube level has remained a challenge due to the small nanotube signal and unavoidable environment background[10–17]. Here, we report high-throughput real-time optical imaging and broadband *in situ* spectroscopy of individual carbon nanotubes on various substrates and in field-effect transistor devices using polarization-based microscopy combined with supercontinuum laser illumination. Our technique enables the complete chirality profiling of hundreds of individual carbon nanotubes, both semiconducting and metallic, on a growth substrate. In devices, we observe that high-order nanotube optical resonances are dramatically broadened by electrostatic doping, an unexpected behaviour that points to strong interband electron–electron scattering processes that could dominate ultrafast dynamics of excited states in carbon nanotubes.

Light polarization is extremely sensitive to minute optical anisotropy in a system, and has long been exploited to study materials ranging from molecules to crystals[18,19]. Manipulation of polarization is especially suitable for the study of carbon nanotubes because of the strong depolarization effect of these one-dimensional structures[20–22]. Figure 1 presents a scheme of our experimental set-up. From an interferometric point of view, the optical contrast of a nanotube in a reflection configuration results from interference between the nanotube-scattered electric field E_{NT} and the substrate-reflected electric field E_r at the detector. This yields an optical contrast

$$\frac{\Delta I}{I} = \frac{|E_r + E_{NT}|^2 - |E_r|^2}{|E_r|^2} = \frac{2|E_{NT}|}{|E_r|}\cos\phi$$

where I is the optical signal from pure substrate reflection, ΔI is the optical signal difference arising from the presence of a nanotube, and ϕ denotes the phase difference between E_{NT} and E_r at the detector. (The $|E_{NT}|^2$ term has been neglected because it is orders of magnitude smaller than the terms involving $|E_{NT}| * |E_r|$.) Therefore, one can, in principle, greatly enhance the nanotube contrast by reducing the reflected electrical field while maintaining the nanotube electrical field. This is achieved by polarization manipulation, as shown in Fig. 1a,b. Horizontally polarized incident light (after polarizer 1) illuminates a nanotube oriented at 45°. The nanotube-scattered electrical field (E^0_{NT}) is polarized along the nanotube direction due to a strong depolarization effect on light polarized perpendicularly to the nanotube, while the substrate reflection (E^0_r) retains the horizontal polarization, with $E^0_{NT}/E^0_r \approx 1 \times 10^{-4}$ (Fig. 1c)[22]. Polarizer 2 is oriented close to the vertical direction (with a small angle deviation δ), which strongly reduces the reflection field to $E_r = E^0_r \sin\delta$, but largely keeps the nanotube field at $E_{NT} = E^0_{NT}/\sqrt{2}$. The nanotube contrast is therefore enhanced by $1/(\sqrt{2}\sin\delta)$, which can reach over 100 with a reasonably small δ and produces $E_{NT}/E_r > \sim 1 \times 10^{-2}$ (Fig. 1d). (For a more detailed description of the optical contrast mechanism see Supplementary Section 1.)

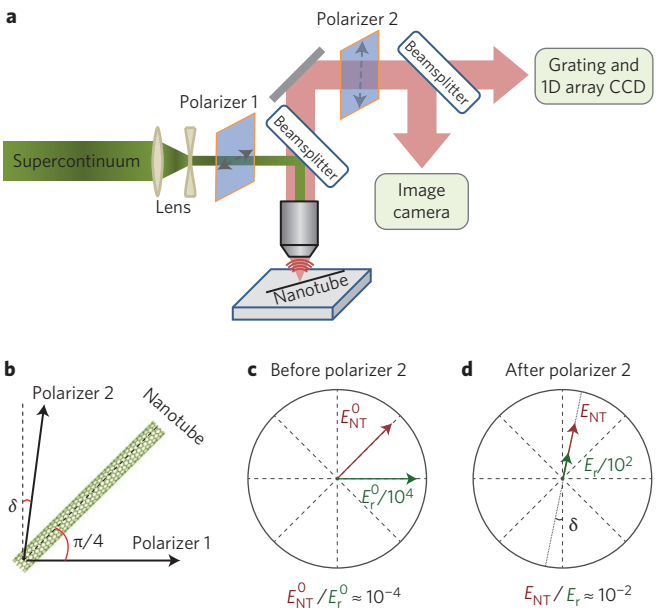

Figure 1 | Scheme of polarization-based optical microscopy for single-nanotube imaging and spectroscopy. a, Combination of supercontinuum laser illumination and high-contrast polarization microscopy for high-throughput individual nanotube imaging and chirality identification. **b**, Configuration of incident polarizer 1, outgoing polarizer 2 and a carbon nanotube. **c**,**d**, Illustration of electrical field polarization before (**c**) and after (**d**) polarizer 2. Dramatic reduction of the reflection electrical field leads to an enhancement of nanotube optical contrast by $\sim 1/(\sqrt{2}\sin\delta)$, where δ is the angle of deviation of polarizer 2 from the perpendicular direction.

[1]Department of Physics, University of California at Berkeley, Berkeley, California 94720, USA, [2]Department of Chemistry, Duke University, Durham, North Carolina 27708, USA, [3]International Centre for Quantum Materials, School of Physics, Peking University, Beijing 100871, China, [4]Materials Science Division, Lawrence Berkeley National Laboratory, Berkeley, California 94720, USA; †These authors contributed equally to this work. *e-mail: fengwang76@berkeley.edu

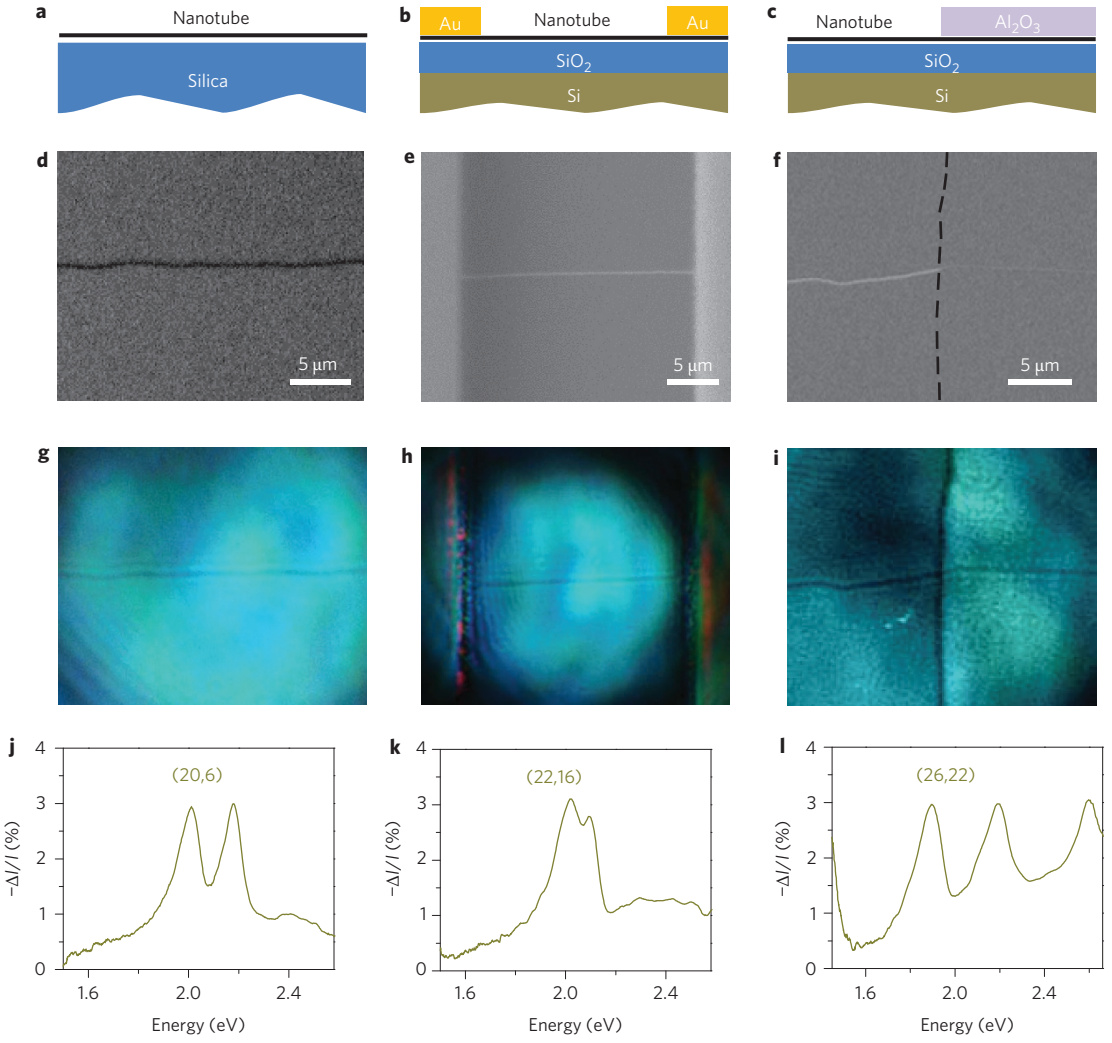

Figure 2 | Optical imaging and spectroscopy of an individual nanotube on substrates and in devices. a–c, Schematics of a nanotube on a fused-silica substrate, a nanotube in a back-gated field-effect transistor device (with two gold electrodes), and a nanotube located partly under an Al_2O_3 dielectric layer. **d–f**, Scanning electron microscopy images of the nanotubes corresponding to the configurations in **a–c**. The dashed line in **f** indicates the invisible Al_2O_3 edge. **g–i**, Direct optical images of the individual nanotubes in **d–f**, obtained using a colour camera and an integration time of ~20 ms. The optical images show high contrast for all individual nanotubes. **j–l**, Optical spectra of the nanotubes in **g–i**, from which we identify that the nanotubes have chiralities of (20,6), (22,16) and (26,22), respectively. These are semiconducting, metallic and semiconducting nanotubes with diameters of 1.8, 2.6 and 3.3 nm, respectively.

Although the concept of polarization enhancement is appealingly simple, its experimental implementation to achieve wide-field imaging and spectroscopy of single nanotubes on substrates has been challenging due to constraints of polarization control in optical microscopy. Indeed, no individual carbon nanotubes on substrates have ever been observed with regular polarization microscopes with high-numerical-aperture (high-NA) objectives, because their polarization extinction is typically on the order of several hundreds[18], too low to achieve sufficient contrast enhancement. Recently, a specialized polarization-based transmission microscopy was used to probe single-nanotube optical absorption[15], but the technique was limited to probing suspended carbon nanotubes with no background from the substrate (as in previous Rayleigh scattering measurements[11–13]). Furthermore, it requires slow frequency scanning with a Ti:sapphire laser.

Our technique simultaneously achieves a polarization extinction ratio of 1×10^5 (more than one order of magnitude higher than a conventional polarization microscope) and a submicrometre spatial resolution in a reflection microscope using polarization control and broadband supercontinuum illumination. It allows us to demonstrate wide-field imaging and high-throughput spectroscopy of individual nanotubes in devices. The most important development in this set-up is separate optimization of the effective NA for nanotube illumination and imaging. A major challenge in polarization microscopy arises because light passing through a large-NA objective becomes strongly depolarized due to polarization-dependent reflection at oblique incidence[23]. However, a large-NA objective is crucial for high-spatial-resolution imaging of nanotubes. In other words, high polarization purity and high spatial resolution seem to be two contradictory requirements. In our experiment, we make use of the fact that high polarization extinction is only required for the reflected light, and spatial resolution can be maintained by collecting the nanotube-scattered light with a large NA. This allows us to satisfy the two requirements simultaneously. Specifically, we use an objective with large NA (0.8), which collects nanotube-scattered light with full NA to obtain high spatial resolution. On the other hand, we control the illumination light to have a much smaller 'effective NA' by using an incident beam with a diameter much smaller than the objective back aperture, as illustrated in Fig. 1a. Here, the incident and reflected light only pass through the centre of the objective and suffer little from polarization degradation due to oblique incidence. This special

illumination scheme exploits the highly collimated beam of a supercontinuum light source, and is critical for achieving high polarization purity and spatial resolution simultaneously in single-tube imaging and spectroscopy. It is also critical to maintain the high polarization purity and a flat spectral response by careful selection of broadband and birefringence-free optical components. This includes using a minimal number of components between the two polarizers, and minimizing the strain for the necessary beamsplitter and objective.

We also exploit several unique aspects of the supercontinuum laser for the high-throughput imaging and spectroscopy of single nanotubes. First, the low coherence of the supercontinuum eliminates the interference and speckles typical for single-wavelength laser illumination. Second, the high brightness of the supercontinuum ensures a large optical signal, even after high extinction from polarization control. Third, the broadband light source enables a single-shot measurement of the whole spectrum.

Our technique enables direct imaging of single nanotubes in diverse configurations, as illustrated schematically in Fig. 2a–c. Figure 2d–f presents corresponding scanning electron micrographs of a nanotube on a fused-silica substrate (Fig. 2d), a nanotube in a back-gated field-effect transistor with source–drain electrodes (Fig. 2e), and a nanotube partly covered by an Al_2O_3 dielectric layer (Fig. 2f). We can image such individual nanotubes directly using optical microscopy (Fig. 2g–i) rather than electron microscopy. A single-walled nanotube typically has a contrast larger than 5% in our optical microscopy images. Supplementary Movie 1 demonstrates the capability of imaging single nanotubes on a substrate in real time. More importantly, we not only 'see' individual nanotubes, but we also obtain their optical spectra and uniquely identify their chiralities. Figure 2j–l displays the spectra of the nanotubes shown in Fig. 2g–i. Each spectrum was obtained within 2 s using broadband supercontinuum illumination and a spectrometer equipped with a linear-array charge-coupled device (CCD). From the prominent optical resonances in the spectra, we can assign chiralities (20,6), (22,16) and (26,22) to these three single-walled nanotubes[12]. These correspond to semiconducting, metallic and semiconducting nanotubes with diameters of 1.8, 2.6 and 3.3 nm, respectively.

Such high-throughput imaging and chirality identification of nanotubes on substrates could be an indispensable tool for improving carbon nanotube growth, because it enables a systematic optimization of nanotube growth conditions. To date, this has not been possible, because there has been no simple and reliable way to accurately determine nanotube chirality and abundance at the same time (except for a rough diameter distribution using resonant Raman measurement[24]). Figure 3 plots the chirality of over 400 single-walled nanotubes from one growth condition (see Methods for growth details), which includes 240 semiconducting nanotubes and 162 metallic nanotubes. The detailed chirality distribution of hundreds of nanotubes on as-grown substrates (transparent or opaque) can therefore be determined accurately. The chirality distribution in Fig. 3a shows that, in this specific sample, semiconducting and metallic nanotubes are enriched in different regions with characteristic chiral angle and diameter dependence. The chiral angle distribution (Fig. 3c) shows that large chiral angles (close to the armchair direction) are more favourable, consistent with previous findings[10]. However, the diameter distribution (Fig. 3b) is quite surprising. It reveals a strong correlation between the diameter and a nanotube being semiconducting or metallic. With a random distribution of chirality, one expects a ratio of 2:1 for semiconducting and metallic nanotubes. However, we observe that for nanotube diameters between 1.7 and 2.1 nm, semiconducting species are highly enriched, and metallic ones completely dominate for nanotube diameters larger than 2.3 nm. This unusual correlation behaviour can only be revealed with our capability to map all individual

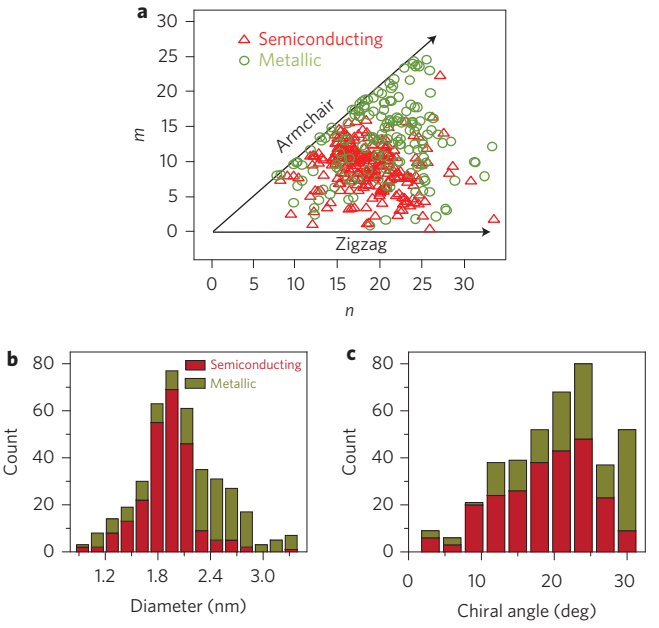

Figure 3 | High-throughput chirality profiling of 402 single-walled carbon nanotubes from one growth condition. a, Chiral index distribution of semiconducting and metallic nanotubes, showing enrichment in different *n*-*m* regions. **b**, Diameter distribution of semiconducting and metallic nanotubes. This reveals a surprising correlation—semiconducting species are highly enriched for nanotube diameters between 1.7 and 2.1 nm, whereas metallic species dominate for tube diameters larger than 2.3 nm. **c**, Chiral angle distribution of semiconducting and metallic nanotubes, showing that large chiral angles (close to the armchair direction) are more favourable, consistent with previous findings[10].

nanotube chiralities on substrates. In comparison, previous Raman characterization and electrical measurements only show an overall enrichment of semiconducting nanotubes in this growth condition, without observing any diameter–metallicity correlation[24], because Raman scattering selectively probes only nanotube species in resonance with the excitation laser and can miss the full picture. The accurate and complete characterization of as-grown nanotube species enabled by our technique will be beneficial for better understanding growth mechanisms and systematic growth optimization.

In situ imaging and spectroscopy of individual nanotubes also offers new opportunities to probe nanotube physics in operating devices. We therefore examined gate-variable nanotube optical transitions in field-effect devices (Fig. 2b) to investigate electron–electron interaction effects on excited states in nanotubes.

Figure 4a,b displays gate-dependent optical spectra for an (18,18) metallic nanotube and a (26,10) semiconducting nanotube, respectively. The resonance peak in metallic (18,18) nanotubes arise from M_{22} transitions, and the peaks in semiconducting (26,10) nanotubes from S_{44} and S_{55} transitions. All these optical resonances show significant broadening with gate voltage varying from close to 0 V to −30 V, which corresponds to nanotube doping from the charge neutral point to a hole density of ∼0.45 e nm^{-1} (based on calibration using G-mode Raman resonance in metallic nanotubes[25]; Supplementary Section 2). At such doping levels, free holes partially fill the linear band of metallic nanotubes or the first subband of semiconducting nanotubes. Accordingly, the broadening of the higher-band optical transition cannot be explained by Pauli blocking dominating semiconducting-nanotube fluorescence or graphene absorption[26,27]. Instead, it originates from many-body interactions between doped carriers and excitons in the carbon nanotubes.

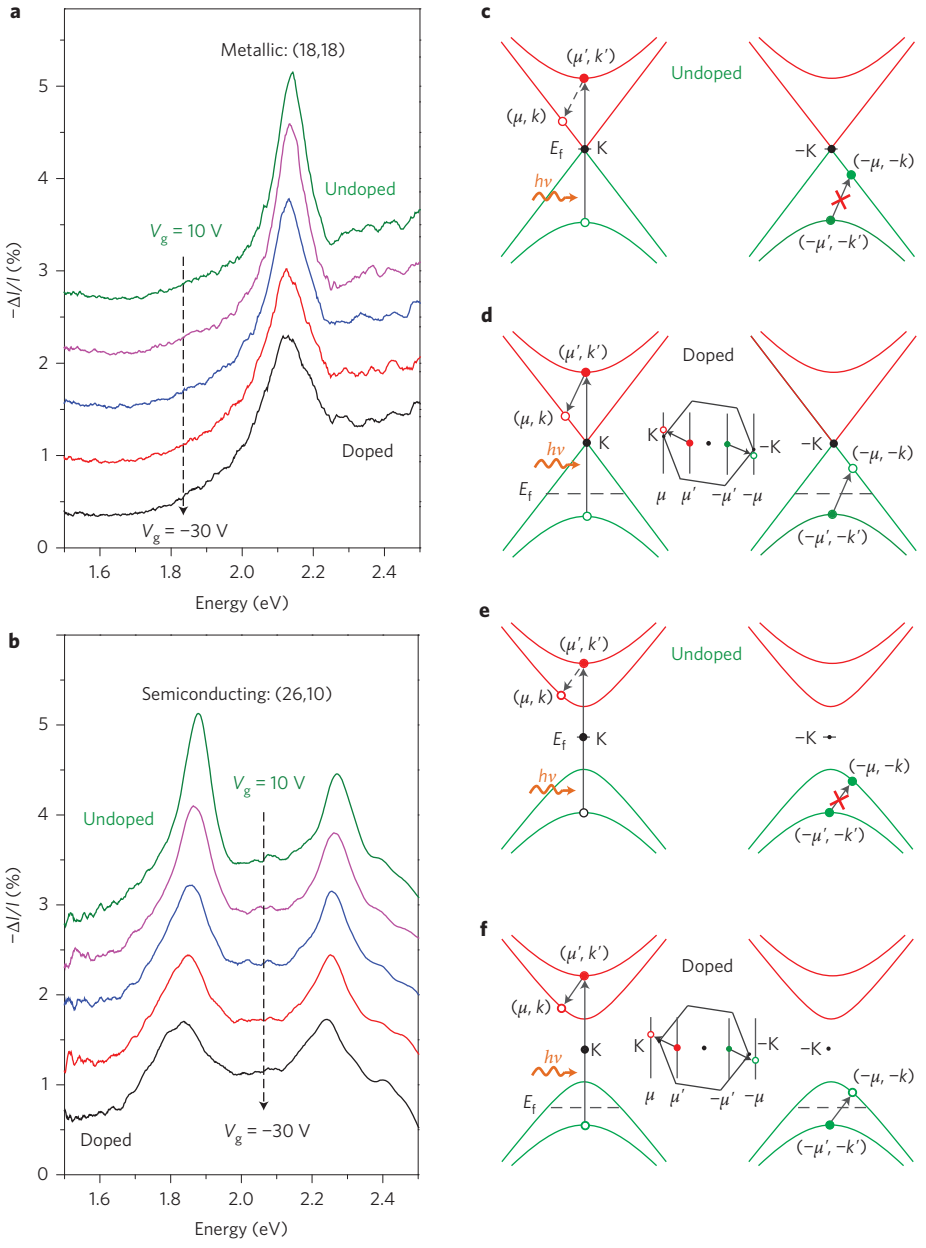

Figure 4 | Gate-variable nanotube optical transitions in field-effect devices. a,**b**, Optical spectral evolution of metallic (18,18) (**a**) and semiconducting (26,10) (**b**) nanotubes under different back-gated voltages. A significant broadening is observed for all transition from $V_g = \sim 0$ V to −30 V, which corresponds to changes from the undoped state to hole doping of ~0.45 e nm^{-1}. At this doping level, free holes partially fill the linear band of the metallic nanotubes or the first subband of the semiconducting nanotubes. **c**–**f**, Schematic illustration of one representative ultrafast decay pathway of an optically excited electron due to intersubband electron–electron scattering in doped metallic (**d**) and semiconducting (**f**) nanotubes. (See supplementary Section 5 for the other three related decay pathways.) The photoexcited electron decays to a state in a lower subband and transfers its energy (E), momentum (k) and angular momentum (μ) to a free hole in the other valley. This process requires a free hole to participate, and it is forbidden for undoped nanotubes (**c** and **e**) but allowed for doped ones (**d** and **f**). Insets (**d**,**f**): the process in the two-dimensional graphene Brillouin zone, where the vertical lines correspond to nanotube subbands (their distance is exaggerated for clarity). It shows that E, k and μ are conserved in this intersubband electron–electron scattering. K and −K represent corner points in the Brillouin zone. E_f, Fermi energy.

Electron–electron interactions can be greatly enhanced in one dimension. Two types of interaction between doped carriers and excitons are known to affect excitonic resonances in nanotubes: dielectric screening[28,29] and the formation of trion states[30]. Trions will lead to a new optical resonance[30], which we do not observe in the higher subband transitions. Dielectric screening of the nanotube exciton is expected to shift the exciton transitions with little increase in the optical linewidth[28], and previous Raman studies suggest that this dielectric screening dominates the gate-induced redshift in excitonic transitions[29]. In our experiment, we do observe a small redshift in most exciton transitions, presumably due to the screening effect. However, the more obvious gate-induced effect is a broadening of exciton resonance linewidth. Linewidth broadening from dielectric screening is expected to be less than 15 meV (see Supplementary Section 3 for more details), but experimentally we observed a gate-induced broadening of more than 50 meV. This large broadening beyond the dielectric screening effect cannot be explained using established mechanisms. Because inhomogeneous broadening in single-nanotube spectra is small (optical spectra taken at significantly different locations along the same tube are almost identical;

for an example see Supplementary Section 4), the resonance width can be directly related to the ultrafast dynamics of an excited state. The observed gate-induced broadening cannot arise from a change in dephasing due to exciton–phonon coupling, because electrical gating mainly introduces free-carrier doping with little effect on exciton–phonon interactions. This indicates that a new type of electron–exciton interaction is critically important.

We propose that intersubband scattering between the exciton and gate-induced free carriers (Fig. 4c–f, Supplementary Section 5) could be responsible for the ultrafast dephasing of excitons through population decay. This electron–electron scattering is an Auger-type process, and it is strongly constrained in one-dimensional carbon nanotubes by the conservation of energy, momentum and angular momentum (described by the quantum number E, k and band index μ, respectively[1]). Figure 4 shows the representative scattering channels that satisfy the stringent conservation requirements in hole-doped metallic (Fig. 4d) and semiconducting (Fig. 4f) nanotubes. Such scattering between optically excited electrons and free holes (in another valley) is absent in pristine undoped carbon nanotubes (Fig. 4c,e), but emerges with hole doping (Fig. 4d,f). (Excitonic correlation between the excited electron and hole, not shown in the illustration for simplicity, should not change the picture qualitatively.) This intersubband electron–electron scattering rate increases with free-carrier concentration, and can dominate ultrafast relaxation of the exciton state with high doping.

It is interesting to note that carbon nanotubes provide a unique opportunity to probe different ultrafast processes in graphitic materials that share similar electronic structures and dynamic responses. Unlike graphene, the well-defined exciton resonances in nanotubes allow one to estimate the ultrafast excited-state dynamics from resonance widths using the Heisenberg uncertainty principle. In addition, the stringent constraint arising from energy, momentum and angular momentum conservation means that excitons can relax only through electron–phonon interactions in undoped nanotubes, allowing us to isolate the electron–phonon interaction contribution to ultrafast dynamics. On the other hand, gate dependence selectively probes the exciton relaxation through electron–electron interactions. If we take the M_{22} transition in an (18,18) nanotube as an example, we can isolate a dephasing rate of approximately $(5\ \mathrm{fs})^{-1}$ from exciton–phonon coupling and a decay rate of approximately $(10\ \mathrm{fs})^{-1}$ from exciton–electron coupling at a doping level of $\sim 0.45\ \mathrm{e\ nm}^{-1}$. Such knowledge of ultrafast relaxation will be important for optoelectronic applications that make use of hot electrons in carbon nanotubes and graphene[31].

In summary, our polarization-based optical microscopy enables a high-throughput imaging and spectroscopy of individual carbon nanotubes on substrates and in devices. As well as carbon nanotubes, the technique can enhance the optical contrast of other 'invisible' anisotropic materials. This capability can open up exciting opportunities in the study of a variety of one-dimensional nanomaterials, including graphene nanoribbons, semiconductor nanowires and nanorods, and nanobiomaterials such as actin filaments.

Methods

Growth of carbon nanotubes on different substrates. Long nanotubes were grown by chemical vapour deposition (CVD) on various substrates, including fused silica, quartz, SiO_2/Si, Si_3N_4/Si and Al_2O_3/SiO_2/Si substrates. For the study of the nanotube device, we typically used methane in hydrogen (CH_4:H_2 = 1:2) as the gas feedstock and a thin film (~0.2 nm) of iron as the catalyst on the SiO_2/Si substrate, for growth at 900 °C (ref. 32). This growth condition yielded nanotubes with spacing of tens of micrometres. For the study of chirality distribution, nanotubes were grown on Y-cut single-crystal quartz substrates at 900 °C (ref. 24). For this growth, we used ethanol plus water through argon bubble (90 s.c.c.m. for ethanol and 30 s.c.c.m. for water at 0 °C) with hydrogen (280 s.c.c.m.) as the gas feedstock and $CuCl_2$/poly(vinylpyrrolidone) alcohol solution as catalysts.

Fabrication of carbon-nanotube devices. The back-gated nanotube field-effect transistor in Fig. 2b was fabricated on a 90 nm SiO_2/Si substrate. Two gold electrodes (thickness, 20 nm) were evaporated onto the nanotube by electron-beam evaporation. The Al_2O_3 layer (thickness, 15 nm) in Fig. 2c was evaporated onto the nanotube by electron-beam evaporation.

Optical measurements. Figure 1a presents a detailed optical set-up of the experiment, which includes a supercontinuum laser (Fianium SC-450), two Glan-Thomspon polarizers (Thorlabs, GTH10), a Nikon objective (NA = 0.80, LU Plan Fluor), an optical grating (300 lines/mm, Thorlabs GTI50-03), a +300/−15 mm lens pair for controlling the illumination beam size, a camera (Nikon 5100) for imaging, and a one-dimensional CCD array (Imaging Solution Group LW-ELIS-1024a-1394) to obtain the spectrum.

The supercontinuum laser (~470–1,800 nm) was used as the light source[11,12]. A reflective microscope was used, the objective of which focused the supercontinuum light to the sample and then collected the nanotube-scattered and substrate-reflected light. One polarizer was located in the incident beam with its transmission axis set horizontally, and a second polarizer was placed in the detection beam, with its polarization set to a small angle δ from the vertical direction.

For nanotube imaging we narrowed the illumination beam through the centre of the microscope to achieve high polarization purity, and used an effective objective NA of ~0.01. This resulted in an illuminated area on the sample of diameter 30 μm, which set the field of view. The polarization extinction for the reflected light was maintained above 1×10^5 for all wavelengths to ensure a sufficient optical contrast of the nanotubes. Images were taken with a Nikon D5100 camera with an integration time of ~20 ms. The movie was taken at a rate of 30 frames per second.

For nanotube spectroscopy we expanded the incident supercontinuum beam and focused it on the sample. We set the illumination beam size with an effective NA of ~0.4, which was the optimal compromise between achieving a smaller focal spot and having higher polarization purity. We periodically modulated the position of the nanotube and measured the spectra with the nanotube inside (I_{inside}) and outside (I_{outside}) the beams. The final spectrum was obtained as $\Delta I/I = (I_{\mathrm{inside}} - I_{\mathrm{outside}})/I_{\mathrm{outside}}$. For this measurement, we used a one-dimensional CCD array to achieve faster readout and a better signal-to-noise ratio.

Nanotube chirality assignment from optical resonances. For each single-walled carbon nanotube spectrum, transition energies at the optical resonance peaks were identified between 1.4 and 2.6 eV. These transition energies were compared to an atlas of suspended nanotube optical transitions to assign the nanotube chirality[12]. To account for the dielectric screening effect from the substrate, a 40 meV redshift was added to the transition energies taken from the atlas[28,33]. For approximately 90% of the single-walled nanotubes with diameters between 0.8 and 3.4 nm, identification was unique. The remainder had two or three possible assignments. However, all possible candidates typically belonged to the same family, with nearly identical diameters. Their physical properties were very similar and this assignment uncertainty will not affect most nanotube studies.

Received 19 July 2013; accepted 1 October 2013;
published online 10 November 2013

References

1. Dresselhaus, M. S., Dresselhaus, G. & Avouris, P. *Carbon Nanotubes: Synthesis, Structure, Properties, and Applications* (Springer, 2001).
2. Javey, A. *et al.* Ballistic carbon nanotube field-effect transistors. *Nature* **424,** 654–657 (2003).
3. Chen, J. *et al.* Bright infrared emission from electrically induced excitons in carbon nanotubes. *Science* **310,** 1171–1174 (2005).
4. Gabor, N. M. *et al.* Extremely efficient multiple electron–hole pair generation in carbon nanotube photodiodes. *Science* **325,** 1367–1371 (2009).
5. Hertel, T. Carbon nanotubes: a brighter future. *Nature Photon.* **4,** 77–78 (2010).
6. Dang, X. N. *et al.* Virus-templated self-assembled single-walled carbon nanotubes for highly efficient electron collection in photovoltaic devices. *Nature Nanotech.* **6,** 377–384 (2011).
7. Lindfors, K., Kalkbrenner, T., Stoller, P. & Sandoghdar, V. Detection and spectroscopy of gold nanoparticles using supercontinuum white light confocal microscopy. *Phys. Rev. Lett.* **93,** 037401 (2004).
8. Celebrano, M., Kukura, P., Renn, A. & Sandoghdar, V. Single-molecule imaging by optical absorption. *Nature Photon.* **5,** 95–98 (2010).
9. Kukura, P., Celebrano, M., Renn, A. & Sandoghdar, V. Imaging a single quantum dot when it is dark. *Nano Lett.* **9,** 926–929 (2008).
10. Bachilo, S. M. *et al.* Structure-assigned optical spectra of single-walled carbon nanotubes. *Science* **298,** 2361–2366 (2002).
11. Sfeir, M. Y. *et al.* Probing electronic transitions in individual carbon nanotubes by Rayleigh scattering. *Science* **306,** 1540–1543 (2004).
12. Liu, K. *et al.* An atlas of carbon nanotube optical transitions. *Nature Nanotech.* **7,** 325–329 (2012).
13. Joh, D. Y. *et al.* On-chip Rayleigh imaging and spectroscopy of carbon nanotubes. *Nano Lett.* **11,** 1–7 (2011).
14. Berciaud, S. *et al.* Absorption spectroscopy of individual single-walled carbon nanotubes. *Nano Lett.* **7,** 1203–1207 (2007).
15. Lefebvre, J. & Finnie, P. Polarized light microscopy and spectroscopy of individual single-walled carbon nanotubes. *Nano Res.* **4,** 788–794 (2011).

16. Jorio, A. *et al.* Structural (*n*, *m*) determination of isolated single-wall carbon nanotubes by resonant Raman scattering. *Phys. Rev. Lett.* **86,** 1118–1121 (2001).
17. Araujo, P. T. *et al.* Third and fourth optical transitions in semiconducting carbon nanotubes. *Phys. Rev. Lett.* **98,** 067401 (2007).
18. Robinson, P. C. & Bradbury, S. *Qualitative Polarized-Light Microscopy* (Oxford Univ. Press, 1992).
19. Fujiwara, H., *Spectroscopic Ellipsometry: Principles and Applications* (Wiley, 2007).
20. Nanot, S. *et al.* Broadband, polarization-sensitive photodetector based on optically-thick films of macroscopically long, dense, and aligned carbon nanotubes. *Sci. Rep.* **3,** 1335 (2013).
21. Miyauchi, Y., Oba, M. & Maruyama, S. Cross-polarized optical absorption of single-walled nanotubes by polarized photoluminescence excitation spectroscopy. *Phys. Rev. B* **74,** 205440 (2006).
22. Islam, M. F. *et al.* Direct measurement of the polarized optical absorption cross section of single-wall carbon nanotubes. *Phys. Rev. Lett.* **93,** 037404 (2004).
23. Brody, J., Weiss, D. & Berland, K. Reflection of a polarized light cone. *Am. J. Phys.* **81,** 24–27 (2013).
24. Zhou, W. W., Zhan, S. T., Ding, L. & Liu, J. General rules for selective growth of enriched semiconducting single walled carbon nanotubes with water vapor as *in situ* etchant. *J. Am. Chem. Soc.* **134,** 14019–14026 (2012).
25. Tsang, J. C. *et al.* Doping and phonon renormalization in carbon nanotubes. *Nature Nanotech.* **2,** 725–730 (2007).
26. O'Connell, M. J., Eibergen, E. E. & Doorn, S. K. Chiral selectivity in the charge-transfer bleaching of single-walled carbon-nanotube spectra. *Nature Mater.* **4,** 412–418 (2005).
27. Wang, F. *et al.* Gate-variable optical transitions in graphene. *Science* **320,** 206–209 (2008).
28. Wang, F. *et al.* Interactions between individual carbon nanotubes studied by Rayleigh scattering spectroscopy. *Phys. Rev. Lett.* **96,** 167401 (2006).
29. Steiner, M. *et al.* Gate-variable light absorption and emission in a semiconducting carbon nanotube. *Nano Lett.* **9,** 3477–3481 (2009).
30. Santos, S. M. *et al.* All-optical trion generation in single-walled carbon nanotubes. *Phys. Rev. Lett.* **107,** 187401 (2011).
31. Xu, X. D. *et al.* Photo-thermoelectric effect at a graphene interface junction. *Nano Lett.* **10,** 562–566 (2010).
32. Huang, S. M., Cai, X. Y. & Liu, J. Growth of millimeter-long and horizontally aligned single-walled carbon nanotubes on flat substrates. *J. Am. Chem. Soc.* **125,** 5636–5637 (2003).
33. Steiner, M. *et al.* How does the substrate affect the Raman and excited state spectra of a carbon nanotube? *Appl. Phys. A* **96,** 271–282 (2009).

Acknowledgements

Nanotube synthesis and optical spectroscopy were supported by a National Science Foundation (NSF) CAREER grant (no. 0846648), the NSF Center for Integrated Nanomechanical Systems (no. EEC-0832819) and NSF grant no. CHE-1213469. Support for device fabrication and characterization instrumentation was provided by the Director, Office of Energy Research, Materials Sciences and Engineering Division, of the US Department of Energy (contract nos. DE-SC0003949 and DE-AC02-05CH11231). J.L. and W.Z. also acknowledge support from Duke SMiF (Shared Materials Instrumentation Facilities).

Author contributions

F.W., K.L. and X.H. conceived the experiment. K.L., X.H. and F.W. carried out optical measurements. X.H. and K.L. carried out electrical measurements. Q.Z., K.L. and A.Z. fabricated and characterized the device. J.L., W.Z. and J.L. grew nanotubes for chirality profiling. K.L., Q.Z. and A.Z. grew nanotubes for the device. C.J., E.G. and F.W. performed the theoretical analysis. All authors discussed the results and wrote the manuscript.

Additional information

Supplementary information is available in the online version of the paper. Reprints and permissions information is available online at www.nature.com/reprints. Correspondence and requests for materials should be addressed to F.W.

Competing financial interests

The authors declare no competing financial interests.